Journal of
Manufacturing and Materials Processing

Article

On the Effect of the Cell Size and Beam Radius on the Compressive Strength and Residual Stresses of Ti-6Al-4V BCC Lattice Sandwich Structures Manufactured by L-PBF

Gaetano Pollara *, Dina Palmeri , Roberto Licari and Antonio Barcellona

Department of Engineering, University of Palermo, Viale Delle Scienze, Edificio 8, 90128 Palermo, Italy; dina.palmeri@unipa.it (D.P.); roberto.licari@unipa.it (R.L.); antonio.barcellona@unipa.it (A.B.)
* Correspondence: gaetano.pollara@unipa.it

Abstract: Lattice structures offer the possibility to obtain lightweight components with additional functionalities, improving their shock absorption and thermal exchange properties. Recently, a body-centered cubic (BCC) lattice structure has been used to fabricate metal lattice sandwich panels (MLSPs) for aerospace applications. MLSPs are made of two external skins and a lattice core and can be produced thanks to laser powder bed fusion technology (LPBF), which is characterized by its superior printing accuracy with respect to other additive manufacturing processes for metals. Since few studies can be found in the literature on Ti-6Al-4V MLSPs, further work is needed to evaluate the mechanical response of these panels. Moreover, due to their design complexity and to avoid a costly experimental campaign, numerical simulation could be used to encourage the industrial application of these structures. In this paper, different cell configurations were printed and tested in compression to study the influence of the cell's geometrical parameters, i.e., the cell size and beam radius, on the mechanical response of MLSPs. Numerical simulations of the LPBF of these geometries were also carried out to understand how the residual stresses can be varied by varying the cell configuration. A geometrical evaluation was carried out to quantitatively express the influence of the beam radius and cell size on the resulting volume fraction, which strongly influences the mechanical behavior and residual stress profiles of MLSPs. From the analysis, we found that the C2-R0.35 sample resulted in the configuration with the highest compressive strength, while C3-R0.25 showed the lowest and most uniform residual stress profile.

Keywords: additive manufacturing; titanium alloys; lattice structures; compression

Academic Editor: Hui Huang

Received: 6 May 2025
Revised: 30 May 2025
Accepted: 6 June 2025
Published: 10 June 2025

Citation: Pollara, G.; Palmeri, D.; Licari, R.; Barcellona, A. On the Effect of the Cell Size and Beam Radius on the Compressive Strength and Residual Stresses of Ti-6Al-4V BCC Lattice Sandwich Structures Manufactured by L-PBF. *J. Manuf. Mater. Process.* **2025**, *9*, 192. https://doi.org/10.3390/jmmp9060192

1. Introduction

The advent of additive manufacturing (AM) has provided new opportunities to design lightweight structures with new functionalities [1–4]. Many industrial sectors, especially the aerospace industry, are interested in manufacturing new components to reduce the weight of structures and, at the same time, improve their performance [5–8]. Since lattice structures are lightweight structures that allow for good thermal exchange and energy absorption capabilities, several studies have been conducted on these structures by academics in the last few years [9–13]. Lattice structures are porous materials that consist of the repetition of an elementary unit cell, and they can be strut-based or defined using a mathematical function. In the first case, the elementary cell is made with several beams that can be oriented and combined differently. In the other case, the elementary cell is based on triply periodic minimal surfaces (TPMSs) such that the mean surface curvature at each point is zero [14]. Many applications can be found in the literature regarding different kinds of lattice structures, such as honeycomb and diamond structures, especially when the 3D printing of polymers is considered [15,16]. Recently, lattice structures, especially body-centered cubic (BCC) structures, have been studied for use as the core of metallic lattice sandwich panels (MLSPs) for aerospace applications [17–19]. These panels consist of two skins and a lattice core of the same material, and they can be produced with laser powder bed fusion (LPBF) technology, characterized by its high accuracy [20]. Since high mechanical strength and corrosion resistance properties are required for aerospace applications, a Ti-6Al-4V alloy can be used [21]. So far, few studies regarding metal lattice sandwich panels can be found in the literature. Wei et al. [19] analyzed the blast response of additive-manufactured Ti-6Al-4V sandwich panels characterized by an auxetic honeycomb lattice core. Numerical simulations were used to predict the mechanical response of MLSPs and show their feasibility for aerospace applications. Aerodynamic loads were investigated by Bici et al. [22] through FEM analysis, considering different design variables such as the cell shape, cell size, beam radius, and shell thickness for Al7075 MLSPs. Unfortunately, no samples were manufactured to validate the optimal results obtained after the individuation of the Pareto front. In [23], Ferro et al. studied the mechanical response of AlSi10Mg lattice sandwich panels manufactured via LPBF. Compressive tests were performed to evaluate the influence of cell shapes (BCC structures with and without vertical struts, also known as BCC-z structures), the cell size, and strut diameters. According to their results, the cell shape and relative density (when the cell type is fixed) are the most influential factors affecting the mechanical response of MLSPs. Guo et al. [24] used a finite element model combined with the Gurson–Tvergaard–Needleman (GTN) damage model to consider the effect of pore defects due to the LPBF process on the compressive strength of AlSi10Mg BCC lattice sandwich panels.

Other applications of lattice sandwich panels can be found in the literature for integration with polymers and composites. Mines et al. [25] addressed drop weight behavior with carbon fiber-reinforced composite (CFRP) skins and a BCC lattice core made of Ti-6Al-4V and 316L stainless steel, manufactured via LPBF. They demonstrated how Ti-6Al-4V is preferred over stainless steel due to its higher specific strength and that it can compete with traditional aluminum honeycomb structures in high-performance aerospace applications when impact performances are considered. Hou et al. [26] compared the energy absorption capacity of auxetic and non-auxetic lattice composites made of two unidirectional CFRP skins and a 3D-printed polymeric core. Sandwich panels consisting of CFRP external face sheets and a polypropylene (PP) honeycomb core were analyzed by Acanfora et al. [27] to obtain efficient shock absorber devices. They showed a better absorption capability compared to full-PP lattice sandwich panels. Wu et al. [28] developed a numerical model to predict the mechanical behavior of polymeric sandwich panels with hierarchical lattice cores when subjected to compression, shearing, and three-point bending.

Even if in the literature it is difficult to find applications of Ti-6Al-4V BCC lattice structures as a core material for MLSPs, they have already been analyzed by academics. Some studies are similar to that of Arputharaj et al. [29], where the authors studied the compression behavior of Ti-6Al-4V manufactured via L-PBF. They analyzed the influence of the beam radius and heat treatment on the compressive response of BCC lattice structures. They emphasize the significance of the volume fraction in determining the mechanical strength of BCC structures and the impact of heat treatment on increasing ductility due to changes in the microstructure and relief from residual stress. It is important to state that the samples' dimensions were varied to have the same number of cells, while in MLSPs the external dimensions should be fixed. Other studies instead focus on the residual stresses and distortion of BCC lattice structures but without considering the numerical simulation of the L-PBF process. In [4], Tian et al. measure the distortion of a cantilever geometry made of BCC unit cells to investigate the effect of the strut diameter and process parameters. In detail, the laser power and scanning pattern showed little influence due to the small size of the deposition area compared to its solid counterpart, while a bigger influence was had by an increase in the strut diameter, which increased the vector length. Due to the long processing time and difficulties in measuring residual stresses, it will be very convenient to develop a numerical model for residual stress prediction. Moreover, the effect of the skin has to be taken into consideration.

Considering the current body of research, further studies are needed to understand the behavior of additive-manufactured metal lattice sandwich panels. In this study, Ti-6Al-4V sandwich panels with a BCC lattice core were manufactured via LPBF to investigate the influence of cell sizes and the beam radius on their mechanical response under compressive load. Moreover, numerical simulations of the printing process were carried out to correlate the mechanical response with the residual stress that can arise during the LPBF process.

2. Materials and Methods

2.1. LPBF of MLSPs for Compression Tests

Metal lattice sandwich panels consist of two solid skins and a lattice core. In this paper, a BCC lattice unit cell was selected to fabricate Ti-6Al-4V lattice sandwich panels. A BCC cell shape was used because it is one of the most analyzed in the literature for this kind of application [17–19]. Moreover, it is easier to design and more customizable [30,31]. BCC elementary unit cells are characterized by two main geometrical parameters, the cell size (C) and beam radius (R). In order to study the influence of cells' geometrical characteristics on the mechanical behavior of MLSPs, four different cases were considered by varying the C and R. The values of C and R were chosen according to a literature review and are reported as follows:

- C = 2 mm or 3 mm;
- R = 0.25 mm or 0.35 mm.

In Table 1, the four cases obtained by combining the selected values for the cell size and the beam radius are reported together with the resulting volume fraction. The samples were named according to the cell dimensions and beam radius used; in other words, if the sample was characterized by C = 2 mm and R = 0.25 mm, we would refer to it as C2-R0.25. Three samples for each cell configuration were printed with external dimensions of 12 mm × 12 mm × 13 mm, a lattice core region of 12 mm × 12 mm × 12 mm, and two external skins of 12 mm × 12 mm × 0.5 mm, as shown in Figure 1a.

Compression samples were fabricated via LPBF with an SLM280HL (Nikon SLM Solutions AG, Lübeck, Germany) 3D system machine. The build platform was preheated up to 200° to reduce the thermal gradient and residual stress [32], and the build chamber was filled with Argon to lower the oxygen content to less than 0.1%. The process parameters were kept the same for each cell configuration. The main process parameters, the laser power (P), scan speed (v), hatch spacing (h), and layer thickness (t), were fixed at 350 W, 1400 mm/s, 120 µm, and 30 µm, respectively. Ti-6Al-4V spherical powder with a Gaussian distribution of 20–63 µm and a density of 4.43 g/cm^3 was adopted to guarantee great corrosion resistance and mechanical strength. The samples were designed with Fusion 360 (Autodesk, San Francisco, CA, USA), while the entire print was designed with Magics (Materialise, Leuven, Belgium), which allow us to perform part orientation, support generation, and all the necessary steps to prepare the slicing file. The parts were oriented so that the skins formed a 90° angle with the titanium build platform in order to reduce distortions due to the residual stresses that would result from the large solid area. The manufactured samples are shown in Figure 1b.

Table 1. Geometrical characteristics of the samples used for the compressive tests.

Sample ID	C (mm)	R (mm)	V_f	Unit Cell	3D Sketch of the Sample
C2-R0.25	2	0.25	0.264	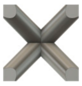	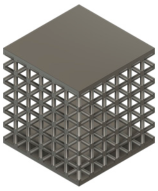
C2-R0.35	2	0.35	0.457	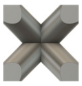	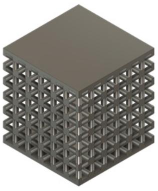
C3-R0.25	3	0.25	0.128	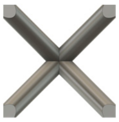	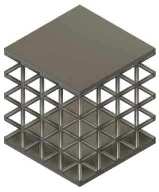
C3-R0.35	3	0.35	0.234	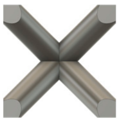	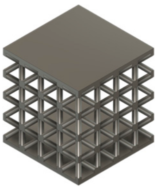

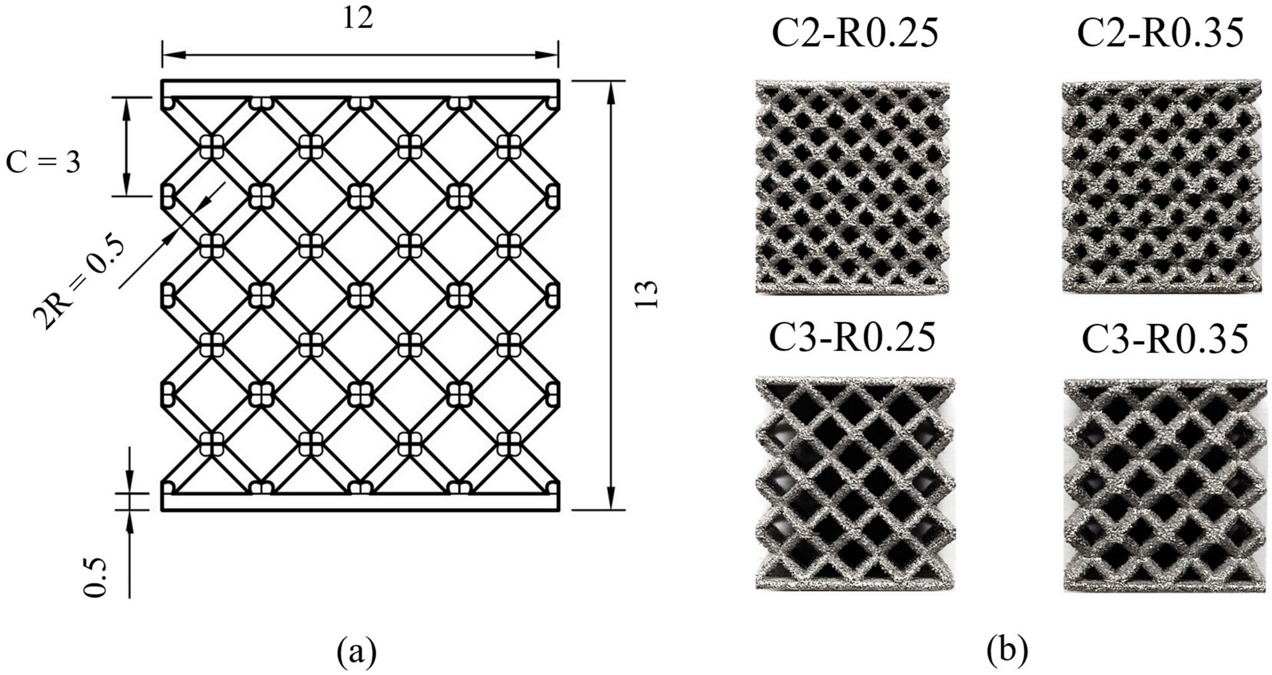

Figure 1. Samples for compression tests: (**a**) 2D sketch with dimensions of front view of C3-R0.25 cell configuration. All units are expressed in mm. (**b**) Picture of 3D-printed samples.

To characterize the mechanical behavior of MLSPs, the printed samples underwent compression tests ($n = 3$ for each cell configuration) on a Quasar 600 (Galdabini, Varese, Italy) universal testing machine with a 600 kN maximum load cell capacity. Compression tests were performed at a constant speed rate of 1 mm/s and using an acquisition rate of 65 Hz.

2.2. Numerical Simulations

In order to evaluate the residual stress generated during the LPBF process, numerical simulations were carried out for each cell configuration. Different approaches can be used when simulating LPBF, such as the microscale, mesoscale, and macroscale approaches. In cases like this, where we want to obtain the residual stress of the entire component due to the AM process, the macroscale approach is usually adopted [33]. Numerical simulations were carried out on Netfabb (Autodesk, CA, USA), a commercial software package based on a finite FEM multi-scale modeling approach which is extremely convenient. In detail, the motion of the laser was predicted at the microscale level; thus, it was possible to predict the local residual stress field at the mesoscale level and finally, using the mesoscale model, to predict the residual stress at the part-scale level. From a practical point of view, the software required the generation of a "parameter file" (PRM) in which all the information regarding the mesoscale level was available for the part-scale simulation. The PRM file could be created within the software, specifying the 3D printing system, deposition strategy (i.e., laser power, scan speed, etc.), and material properties. Using the PRM file as an input for the macroscale simulation gave us a great advantage since it was unnecessary to calibrate the model [34,35].

Temperature-dependent material properties such as the thermal conductivity (k) and specific heat capacity (C_p) used for the thermal analysis are reported in Table 2. According to the work of Sih et al. [36], powder properties can be scaled based on the bulk material properties. In detail, the bulk thermal conductivity was scaled by 1×10^{-2}, the bulk elastic modulus by 1×10^{-4}, and the bulk thermal emissivity by 1.8.

Table 2. Thermal properties of Ti-6Al-4V.

T [°C]	C_p (J/kg)	k (W/m/°C)
0	565	6.6
20	565	6.6
93	565	7.3
205	574	9.1
315	603	10.6
425	649	12.6
540	699	14.6
650	770	17.5
760	858	17.5
870	959	17.5

The temperature-dependent mechanical properties were also used to perform the mechanical analysis and obtain residual stress distributions. In particular, the yield stress (σ_y), Young's modulus, (E), and the coefficient of thermal expansion (α) are shown in Table 3. A constant Poisson's ratio of 0.34 was selected, and the model assumed perfect plasticity.

Table 3. Mechanical properties of Ti-6Al-4V.

T [°C]	σ_y (MPa)	E (GPa)	α (µm/m°C)
0	777.15	105.00	8.60
20	768.15	103.95	8.64
250	664.65	91.81	9.20
500	552.15	78.63	9.70
800	417.15	62.80	9.70

The governing equation used to solve the thermal problem, as well as the governing stress equilibrium for the mechanical analysis, is well known and can be found in [35,37,38]. For the part-scale numerical simulation, the initial substrate ($T_{substrate}$) and build chamber temperatures ($T_{chamber}$) were set at 200 °C and 25 °C, respectively. Moreover, the conduction to the powder was modeled artificially through a convective boundary condition on the model surface by using a convection coefficient of $h = 25\ W/m^2/°C$. Regarding the mechanical analysis, the build plate was fixed, and all the nodes in contact with the substrate were constrained. The nodes were released only to consider the effect of removing the part from the base. The principal boundary conditions are summarized in Table 4.

Table 4. Boundary conditions used for the part-scale simulation.

Boundary Conditions	Description
Mechanical	fixed build plate, no translation or distortion of the substrate is allowed
Thermal	$T_{substrate} = 200\ °C$ $T_{chamber} = 25\ °C$ heat loss to the powder is simulated by assigning a convection coefficient value ($h = 25\ W/m^2/°C$) to the part surfaces

During the part-scale simulation, a voxel mesh characterized by 8-node hexahedral elements was used for the element activation according to the deposition strategy. Usually, in order to reduce the computational time, more real layers are grouped in the computational layer. In this case, 10 real layers were included in each voxel mesh layer. The resulting mesh is shown in Figure 2.

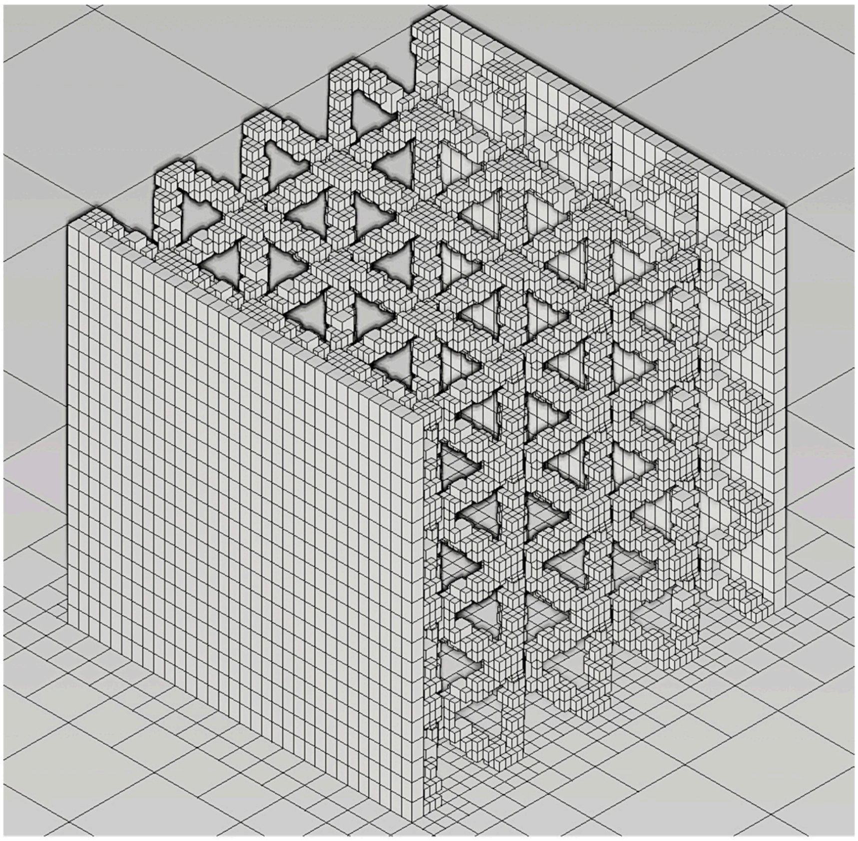

Figure 2. Voxel mesh generated in the case of the C3-R0.25 cell configuration.

3. Results and Discussion

3.1. Mechanical Behavior of MLSPs Under Compressive Load

Compression tests were carried out for each cell configuration to study the mechanical response of the metal lattice sandwich panels. In Figure 3, the compressive strain–stress curve for the C3R0.25 cell configuration shows the generic behavior of the tested samples characterized by a lattice core region.

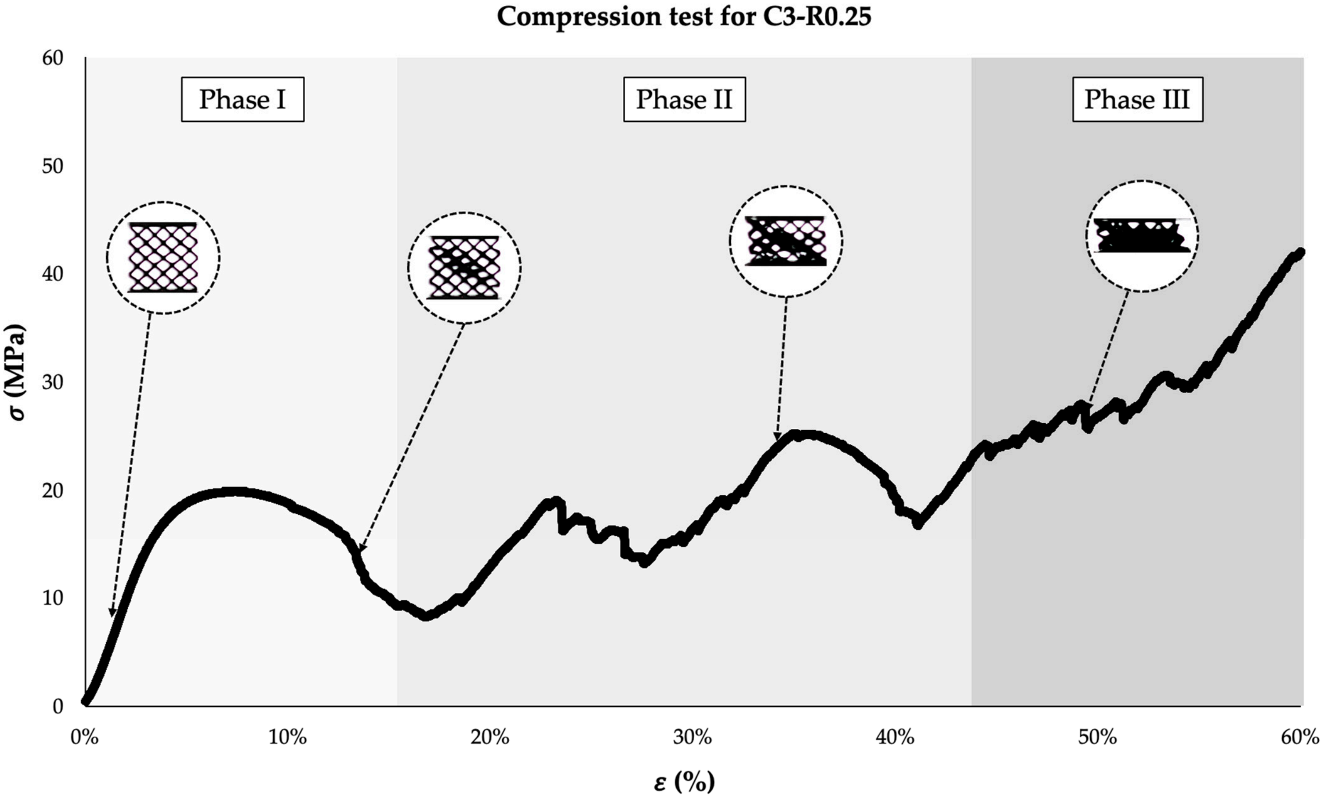

Figure 3. Stress–strain curve from the compression test carried out for the C3-R0.25 cell configuration.

It can be noted how these structures were mainly characterized by three phases when subjected to a compressive load: (i) typical stress–strain curves for the compression test until the first lattice structure collapsed; (ii) the alternating increasing and decreasing of the load due to the continuous densification and collapse of the structure; (iii) only densification, where the loads continuously increased and the structure had completely collapsed. It is interesting to observe how the failure of the lattice structure occurred in most cases along a 45° plane with respect to the loading direction due to the generation of shear bands. These bands developed because of the localized severe deformation of the struts in a specific plane. The occurrence of shear bands was reflected by the unstable compressive stress, which reduced the lattice energy absorption capacity [31,39].

Even if compressive tests were conducted until the densification phenomena occurred, only phase I on the stress–strain curves was considered to compare the mechanical response of the samples by varying the cell configuration. Only phase I was taken into consideration because, from a compressive strength point of view, the failure of the structure had already occurred. After phase I, the increase and decrease in the compressive strength were due to the continued collapsing and densification of the structure. The results for phase I of all the tested samples are shown in Figure 4.

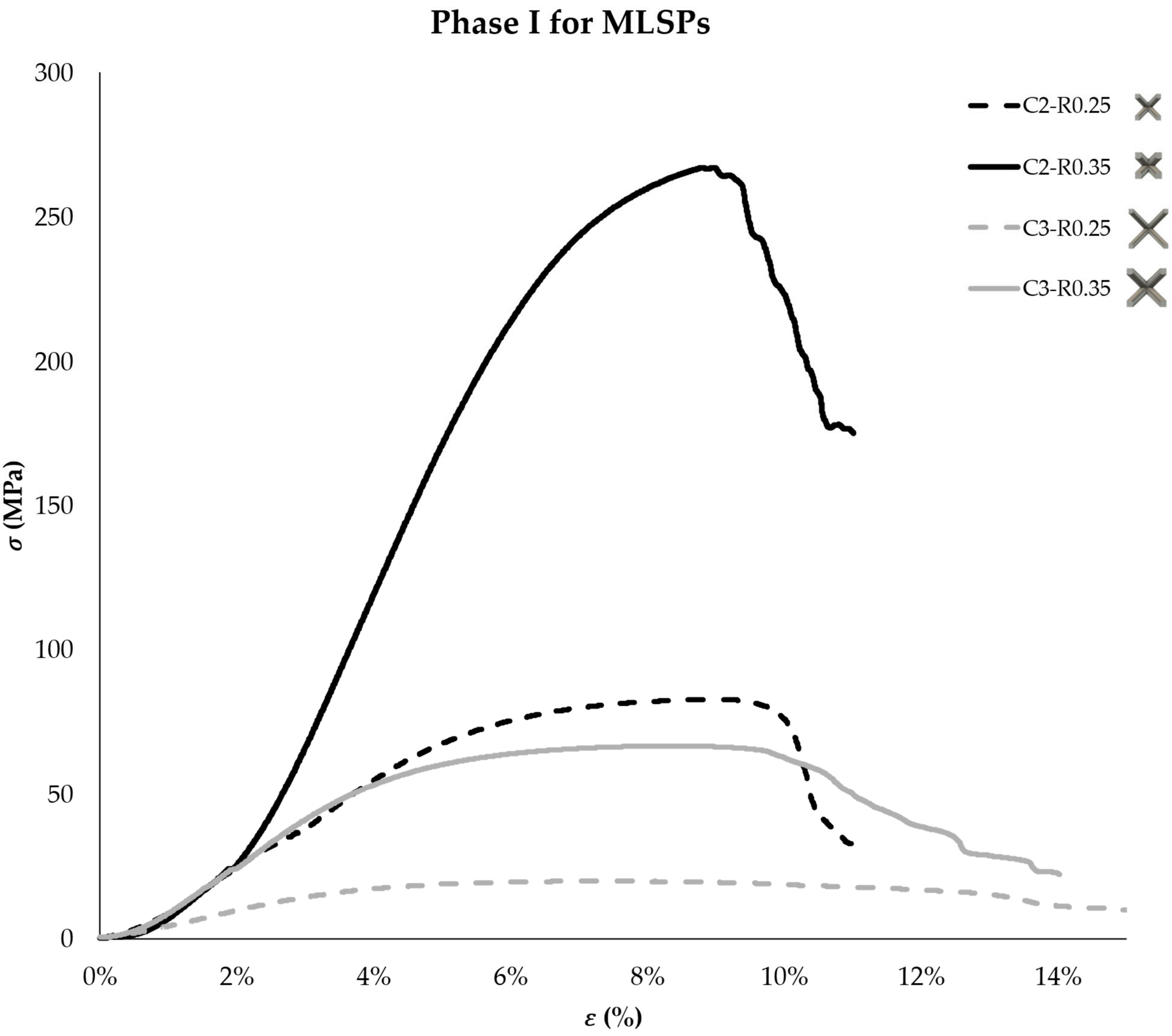

Figure 4. Phase I on the stress–strain curve from the compression test carried out for the C2-R0.25, C2-R0.35, C2-R0.25, and C3-R0.25 samples.

The compressive strength was calculated considering an apparent resisting area of 12 mm × 12 mm for all the samples. From Figure 4, it is clear that the cell size and beam radius play a fundamental role in the compressive strength of MLSPs. Specifically, increasing the beam radius led to an increase in the mechanical strength for both the C2 and C3 cell sizes. This was due to a higher volume fraction with an increasing beam radius. When the beam radius was kept fixed and the cell size increased, a significant decrease in the compressive strength was observed. To explain this, we can roughly visualize the single beam as a small cylinder with a volume, v_b, expressed as follows (Equation (1)):

$$v_b \propto \pi R^2 h = \frac{\pi R^2 C\sqrt{3}}{2} \tag{1}$$

where $h = C\sqrt{3}/2$ is the length of the single beam, which corresponds to half of the cube diagonal. So, an increase in both R and C leads to an increase in the single beam's volume, as reported in Table 5. On the other hand, an increase in the cell size results in a strong reduction in the number of unit cells within the lattice region.

Table 5. Information on the resulting unit cell volume, lattice region volume, and number of unit cells for each sample. The sample volume and unit cell volume were measured from the CAD model.

ID	Total Sample Volume (v_t) [mm^3]	Skins' Volume (v_s) [mm^3]	Sample Volume (v) [mm^3]	Lattice Region Volume (v_l) [mm^3]	Unit Cell Volume (v_c) [mm^3]	Number of Unit Cells (n_c)	Volume Fraction (v_f)
C2-R0.25	1872	144	599.398	455.398	2.108	216	0.264
C2-R0.35	1872	144	932.879	788.879	3.652	216	0.457
C3-R0.25	1872	144	365.995	221.995	3.469	64	0.128
C3-R0.35	1872	144	548.384	404.384	6.319	64	0.234

The number of unit cells (n_c) can be calculated as the ratio between the total volume of the lattice region (v_{lt}) and the total unit cell volume ($v_{ct} = C^3$). The expression "total" is used to refer to the volume which would be occupied if the considered region was fully dense. Otherwise, we are referring to the effective volume occupied in the considered region. Hence, the total volume of the lattice region (v_{lt}) is the difference between the total sample volume (v_t) and the volume occupied by the skins (v_s), as established in Equation (2):

$$n_c = \frac{(v_t - v_s)}{v_{ct}} = \frac{v_{lt}}{v_{ct}} \tag{2}$$

For this reason, if we keep C = 2 mm and change the beam radius from R = 0.25 mm to R = 0.35 mm, we will have an increase in the unit cell volume and the corresponding lattice volume of around 70%. If we keep the beam radius constant and increase the cell size from C = 2 mm to C = 3 mm, we will have an increase in the unit cell volume of 65%, but we will have less material because there will be space for only 64 cells instead of 216. In detail, moving from C2 to C3 resulted in a 70% reduction in the number of cells. This means that by knowing the C2-R0.25 lattice volume ($v_{l(C2-R0.25)}$), we could obtain the C2-R0.35 lattice volume ($v_{l(C2-R0.35)}$) and the C3-R0.25 lattice volume ($v_{l(C3-R0.25)}$), as expressed in Equations (3) and (4):

$$v_{l(C2-R0.35)} = v_{l(C2-R0.25)}\left(1 + \frac{v_{c(C2-R0.35)} - v_{c(C2-R0.25)}}{v_{c(C2-R0.25)}}\right) \tag{3}$$

$$v_{l(C3-R0.25)} = \left(v_{l(C2-R0.25)}\left(1 + \frac{v_{c(C2-R0.35)} - v_{c(C2-R0.25)}}{v_{c(C2-R0.25)}}\right)\right)\left(1 - \frac{n_{c(C2-R0.35)} - n_{c(C2-R0.25)}}{n_{c(C2-R0.25)}}\right) \tag{4}$$

Overall, the best configuration in terms of the compressive strength was C2-R0.35 with a maximum compressive strength of 267 MPa, followed by C2-R0.25 with 83 MPa, C3-R0.35 with 67 MPa, and C3-R0.25 with 20 MPa.

A two-way ANOVA allowed us to analyze not only the main effects of the two independent factors, i.e., the effects of the size of the elementary cell and the beam radius on the dependent variable, the compressive strength of the sandwich panel, but also how these factors interacted with each other. An interaction between two factors meant that the effect of one factor on the compression strength depended on the level of the other factor. The interactions are shown in Figure 5, where in Figure 5a,b the means for each level of one of the factors are displayed according to the levels of the other factor. The lines in Figure 5c are not parallel, indicating the presence of a simple (non-crossover) interaction between the size of the unit cell and the beam radius and the dependent variable, the compressive strength. Finally, both factors were significant because the means of their respective categories were different. The analysis specifically indicated that the compressive strength of the panels showed a notable increase with the value of the beam radius, particularly when the cell dimensions were smaller.

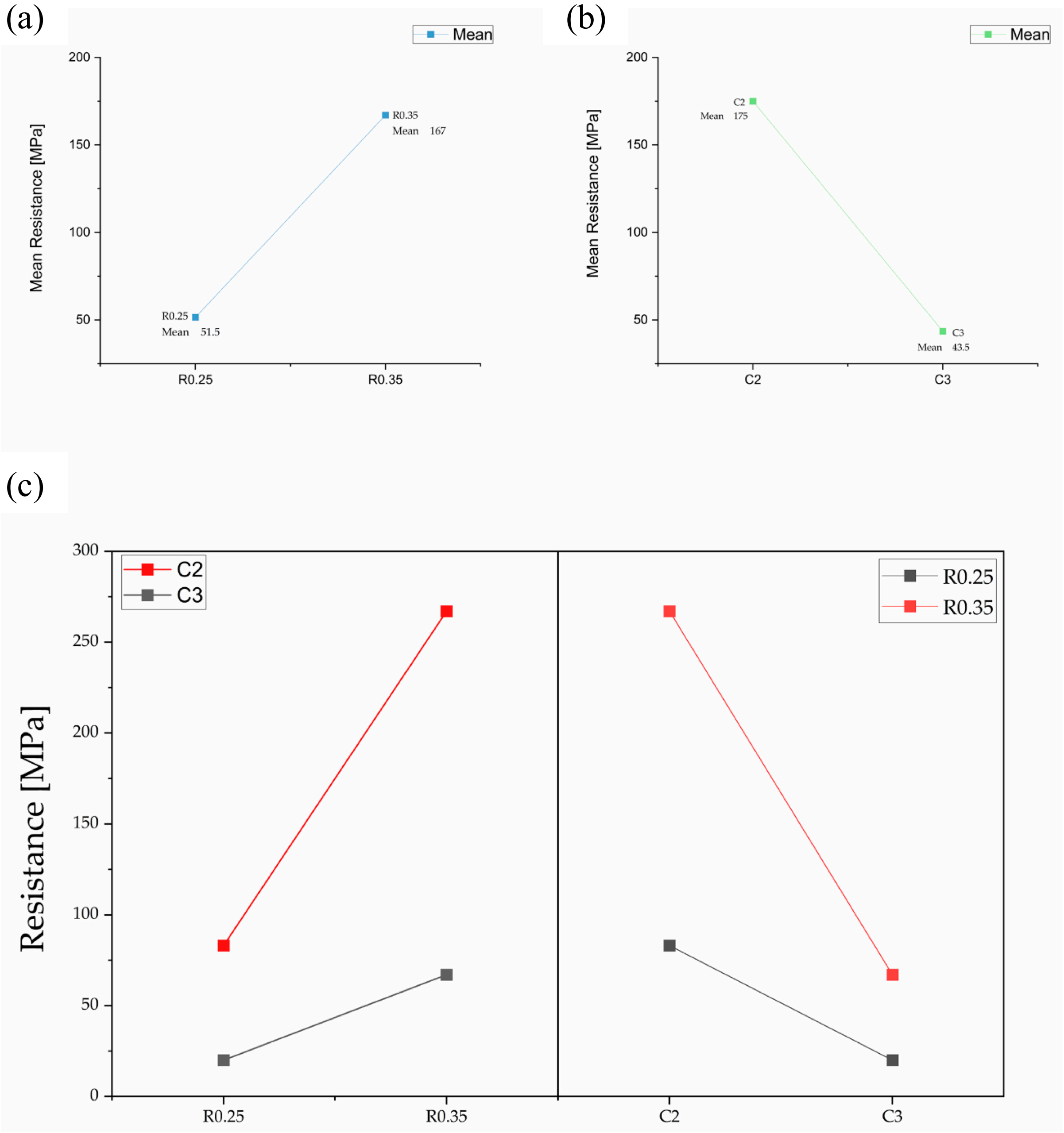

Figure 5. ANOVA of the experimental results: (**a**,**b**) the means for each level of the beam radius and cell size, respectively, and (**c**) the simple (non-crossover) interaction between the size of the unit cell and the beam radius and the dependent variable, the compressive strength.

It has been shown that an increase in the compressive strength is mostly correlated with an increase in the volume fraction, which strongly influences the stiffness of the entire structure. Samples with a lower volume fraction have less material available to withstand the applied load. As a consequence, the stress concentration at the nodes will be more severe, reducing the mechanical strength of the entire structure [29]. Further considerations can be made regarding the effect of the beam radius and cell size on the stiffness of an MLSP. According to the Euler buckling theory [40], the critical load that will cause a column (strut) to fail depends on the slenderness ratio (L_e/R), as established in Equation (5):

$$P_{cr} = \frac{\pi^2 E}{(L/R)^2} = \frac{\pi^2 E}{\left(C\sqrt{3}/2R\right)^2} \tag{5}$$

where L is equal to $C\sqrt{3}/2$, as established in Equation (1), if we consider the single strut as a small cylinder whose length corresponds to half of the diagonal of the cube of length C in which the unit cell is inscribed. A smaller slenderness ratio, i.e., a small cell size or high beam radius, will increase the critical load that the cell can bear. This is in line with the higher compressive strength obtained for the C2-R0.35 MLSPs, which presented the smallest C value and the highest R among the analyzed cell configurations. This also explains the increase in the compressive strength when R increased, while a decrease in the mechanical strength was observed when increasing C.

3.2. Numerical Simulation and Residual Stress Prediction for MLSPs

Multi-step numerical simulations were carried out on Netfabb to predict the residual stresses during the LPBF of MLSPs with changes in the cell configuration. The residual stresses along the X-direction are shown in Figures 6 and 7. The samples were oriented as for the printing process and the Cauchy stresses along the X-direction were considered because they can affect the mechanical properties during compression tests. Since compressive tests were performed by placing the sample skin perpendicular to the universal testing machine axis, the X-residual stress component was in opposition to the compressive load, which was oriented along the same axis.

It can be noticed how the residual stress profiles were more uniform for the C3 cell configuration in comparison to the C2. Moreover, the residual stresses were increased by increasing the beam radius for both the C2 and C3 cell configurations. This was due to the increase in the sample volume, which increased the thermal modulus and created more discrepancies along the z-axis. In detail, the material near the plate will cool rapidly, while the material above will have more difficulty regarding thermal exchange. The numerical simulations show that the C3-R0.25 cell configuration is the most adequate under thermal exchange conditions and residual stresses. This is because, besides having the lowest volume fraction, it has the greatest thermal exchange surface. Table 6 reports the maximum and minimum values for the residual stresses along the X-direction for the simulated samples. It can be observed that the highest tensile residual stress of 917 MPa was found for the C2-R0.35 sample, which was the one with the highest volume fraction, while the lowest value of 542 MPa was found for the C3-0.25 sample, which had the lowest volume fraction. A correlation between the compressive strength and the residual stresses obtained from the numerical simulation can be observed. In detail, when positive residual stresses were more distributed throughout the specimen, higher compressive strength occurred, as for the C2-R0.35 sample. When positive residual stresses were only distributed along the extremities of the specimens, the compressive strength instead presented lower values, as for C2-R0.25 and C3-R0.35. Finally, for a very low volume fraction, no significant residual stress distribution was observed, as for C3-R0.25 (see Figures 6 and 7).

To assess the impact of residual stresses on the long-term performance of MLSPs, such as their fatigue performance, a more systematic study should be carried out. It can be assumed that, due to the higher probability of observing local stresses, residual stresses can influence fatigue crack initiation and propagation [41]. Nevertheless, it has been shown that the influence of the microstructure and defects is greater than that of residual stress for solid samples when considering fatigue properties [42]. This implies that further studies are needed to evaluate the influence of residual stresses on the fatigue performance of lattice structures.

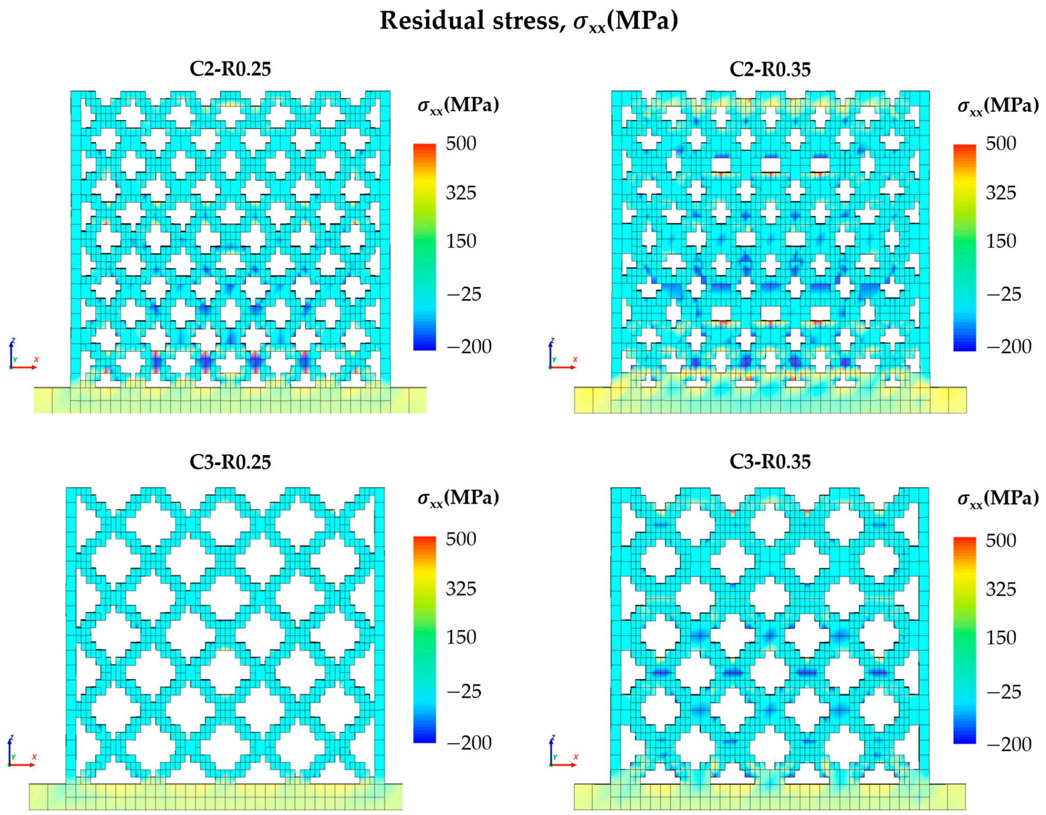

Figure 6. Residual stresses along the X-direction at the end of the printing process obtained with different unit cell configurations.

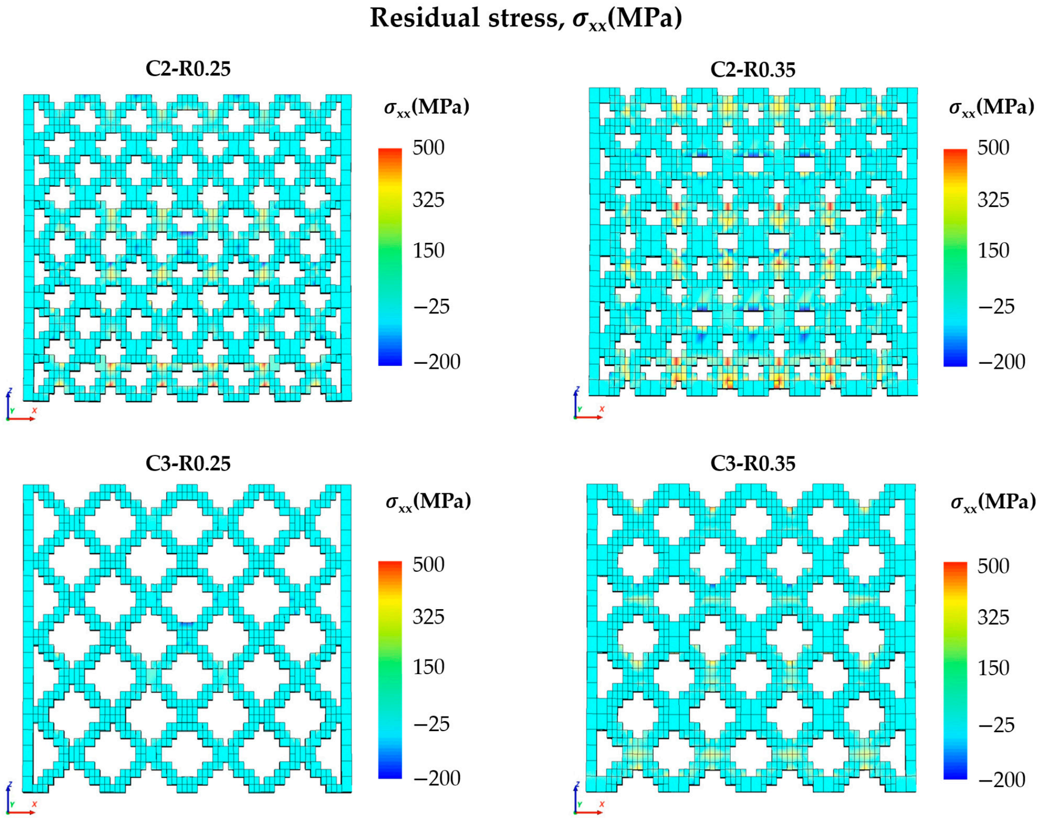

Figure 7. Residual stresses along the X-direction after part removal from the build plate obtained with different unit cell configurations.

Table 6. Maximum and minimum values of residual stresses for the printed MLSPs after the LPBF process and after the samples' removal from the build plate, along the X-direction.

ID	After the Printing Process		After the Samples' Removal	
	Maximum [MPa]	Maximum [MPa]	Maximum [MPa]	Minimum [MPa]
C2-R0.25	725	−498	593	−470
C2-R0.35	917	−559	737	−615
C3-R0.25	542	−328	338	−292
C3-R0.35	660	−446	722	−586

4. Conclusions

In this paper, Ti-6Al-4V MLSPs with different cell configurations were fabricated via LPBF and tested under compressive load to study their mechanical behavior. Moreover, numerical simulations of the printing process were carried out to assess the influence of the cell configuration on the residual stresses. The main findings can be summarized as follows:

- MLSPs, when subjected to compressive load, show three different phases in their stress–strain curve: the initial elasto-plastic deformation of the lattice, followed by the alternation of peaks and valleys due to the alternation of densification and strut failure, and final densification, where the stress continuously increases.
- The cell size and beam radius strongly affect the mechanical behavior of MLSPs. This is due to their direct influence on the sample volume fraction. Specifically, when a high beam radius and small cell size are used, as for the C2-R0.35 samples, high compressive strength will be obtained.
- A mathematical formulation has been introduced to evaluate the volume variation depending on the geometrical parameters of the unit cell.
- The cell configuration also influences the residual stresses generated during the LPBF process. The C3-R0.25 cell configuration had the lowest volume fraction, which facilitated thermal exchange, resulting in a more uniform residual stress profile.
- In conclusion, a geometrical formulation has been provided to evaluate the effect of the beam radius and cell size on the volume fraction, which is one of the most influential factors in the compressive strength of TI-6Al-4V MLSPs. Moreover, an efficient numerical model has been proposed to predict the residual stresses in this kind of structure. These tools can be used by engineers in the design phase of MLSPs, saving them time and costs incurred due to the usual experimental campaign.

5. Research Limitations and Future Developments

Even if numerical simulations were performed to analyze residual stresses and their influence on the compression strength of MLSPs, other factors such as the surface roughness and microscopic defects were not considered in this study. In the future, a more comprehensive study can be carried out to confirm the presented results. Also, a more structured validation phase should be included to confirm the numerical results, which were assumed to be reasonable due to the multi-step modeling nature of the Netfabb simulation software and its proven accuracy in other studies in the literature. Finally, the effect of the process parameters and loading rates on the mechanical response of MLSPs can be investigated in future work.

Author Contributions: Conceptualization, D.P., A.B. and G.P.; methodology, D.P., G.P. and A.B.; software, G.P. and R.L.; validation, D.P., G.P. and R.L.; formal analysis, R.L.; investigation, R.L.; writing—original draft preparation, D.P. and G.P.; writing—review and editing, D.P., G.P., R.L. and A.B.; supervision, A.B. All authors have read and agreed to the published version of the manuscript.

Funding: This research received no external funding.

Data Availability Statement: The data is contained within the article.

Conflicts of Interest: The authors declare no conflicts of interest.

Abbreviations

The following abbreviations are used in this manuscript:

AM	Additive manufacturing
BCC	Body-centered cubic
CFRC	Carbon fiber-reinforced composite
LPBF	Laser powder bed fusion
MLSPs	Metal lattice sandwich panels
TPMS	Triply periodic minimal surface

References

1. Gülcan, O.; Simsek, U.; Cokgunlu, O.; Özdemir, M.; Şendur, P.; Yapici, G.G. Effect of Build Parameters on the Compressive Behavior of Additive Manufactured CoCrMo Lattice Parts Based on Experimental Design. *Metals* **2022**, *12*, 1104. [CrossRef]
2. Rahmani, R.; Bashiri, B.; Lopes, S.I.; Hussain, A.; Maurya, H.S.; Vilu, R. Sustainable Additive Manufacturing: An Overview on Life Cycle Impacts and Cost Efficiency of Laser Powder Bed Fusion. *J. Manuf. Mater. Process.* **2025**, *9*, 18. [CrossRef]
3. De Leon, E.; Riensche, A.; Bevans, B.D.; Billings, C.; Siddique, Z.; Liu, Y. A Review of Modeling, Simulation, and Process Qualification of Additively Manufactured Metal Components via the Laser Powder Bed Fusion Method. *J. Manuf. Mater. Process.* **2025**, *9*, 22. [CrossRef]
4. Tian, Y.; He, J.; Ren, H.; Zha, X.; Lin, K.; Zhou, M.; Xiong, Y. Effect of Process and Geometric Parameters on Residual Distortion of Ti-6Al-4V Body-Centered Cubic Lattice Structures in Laser Powder Bed Fusion. *Addit. Manuf. Front.* **2024**, *3*, 200170. [CrossRef]
5. Blakey-Milner, B.; Gradl, P.; Snedden, G.; Brooks, M.; Pitot, J.; Lopez, E.; Leary, M.; Berto, F.; du Plessis, A. Metal Additive Manufacturing in Aerospace: A Review. *Mater. Des.* **2021**, *209*, 110008. [CrossRef]
6. Imbalzano, G.; Tran, P.; Ngo, T.D.; Lee, P.V. Three-Dimensional Modelling of Auxetic Sandwich Panels for Localised Impact Resistance. *J. Sandw. Struct. Mater.* **2017**, *19*, 291–316. [CrossRef]
7. Dong, L. Mechanical Responses of Ti-6Al-4V Cuboctahedral Truss Lattice Structures. *Compos. Struct.* **2020**, *235*, 111815. [CrossRef]
8. Li, P.; Yang, F.; Liu, Y.; Bian, Y.; Zhang, S.; Wang, L.; Fan, H. Design of Dual-Phase Lattice Materials with Balanced Modulus, Strength and Energy Absorption Properties Based on Sudoku Arranged Reinforcement Phase Distribution. *Comput. Struct.* **2023**, *286*, 107093. [CrossRef]
9. Chen, L.-Y.; Liang, S.-X.; Liu, Y.; Zhang, L.-C. Additive Manufacturing of Metallic Lattice Structures: Unconstrained Design, Accurate Fabrication, Fascinated Performances, and Challenges. *Mater. Sci. Eng. R Rep.* **2021**, *146*, 100648. [CrossRef]
10. Zhumabekova, A.; Toleubekova, M.; Pham, T.T.; Talamona, D.; Perveen, A. Effect of Lattice Structure on Mechanical Properties of Ti-6Al-4V-Ta Alloy for Improved Antibacterial Properties. *J. Manuf. Mater. Process.* **2024**, *8*, 133. [CrossRef]
11. Şimşek, U.; Gülcan, O.; Günaydın, K.; Tamer, A. Prediction of Compressive Behavior of Laser-Powder-Bed Fusion-Processed TPMS Lattices by Regression Analysis. *J. Manuf. Mater. Process.* **2024**, *8*, 16. [CrossRef]
12. Rashid, R.; Masood, S.; Ruan, D.; Palanisamy, S.; Huang, X.; Rahman Rashid, R.A. Design Optimization and Finite Element Model Validation of LPBF-Printed Lattice-Structured Beams. *Metals* **2023**, *13*, 184. [CrossRef]
13. Adelmann, B.; Hellmann, R. Mechanical Properties of LPBF-Built Titanium Lattice Structures—A Comparative Study of As-Built and Hot Isostatic Pressed Structures for Medical Implants. *Metals* **2022**, *12*, 2072. [CrossRef]
14. Benedetti, M.; du Plessis, A.; Ritchie, R.O.; Dallago, M.; Razavi, S.M.J.; Berto, F. Architected Cellular Materials: A Review on Their Mechanical Properties Towards Fatigue-Tolerant Design and Fabrication. *Mater. Sci. Eng. R Rep.* **2021**, *144*, 100606. [CrossRef]
15. Almonti, D.; Salvi, D.; Ucciardello, N. Optimization of Printing Parameters for Polyethylene Terephthalate Glycol Thin Honeycomb Structures with Shape-Memory Behaviors. *Int. J. Adv. Manuf. Technol.* **2025**, *136*, 4455–4469. [CrossRef]
16. Dwivedi, K.; Joshi, S.; Nair, R.; Sapre, M.S.; Jatti, V. Optimizing 3D Printed Diamond Lattice Structure and Investigating the Influence of Process Parameters on Their Mechanical Integrity Using Nature-Inspired Machine Learning Algorithms. *Mater. Today Commun.* **2024**, *38*, 108233. [CrossRef]
17. Wei, K.; Yang, Q.; Yang, X.; Tao, Y.; Xie, H.; Qu, Z.; Fang, D. Mechanical Analysis and Modeling of Metallic Lattice Sandwich Additively Fabricated by Selective Laser Melting. *Thin-Walled Struct.* **2020**, *146*, 106189. [CrossRef]

18. Georges, H.; Großmann, A.; Mittelstedt, C.; Becker, W. Structural Modeling of Sandwich Panels with Additively Manufactured Strut-Based Lattice Cores. *Addit. Manuf.* **2022**, *55*, 102788. [CrossRef]
19. Wei, Y.; Zhang, C.; Yuan, Y.; Chen, P.; Huang, C.; Li, J.; Yuan, M. Blast Response of Additive Manufactured Ti–6Al–4V Sandwich Panels. *Int. J. Impact. Eng.* **2023**, *176*, 104553. [CrossRef]
20. Gibson, I.; Rosen, D.; Stucker, B. *Additive Manufacturing Technologies: 3D Printing, Rapid Prototyping, and Direct Digital Manufacturing*, 2nd ed; Springer: New York, NY, USA, 2015; ISBN 9781493921133.
21. Pupillo, D.; Di Franco, F.; Palmeri, D.; Pollara, G.; Buffa, G.; Fratini, L.; Santamaria, M. Surface Treatments on 3D Printed Ti6Al4V Biomedical Plates to Enhance Corrosion Resistance in Simulated Physiological Solutions and Under Inflammatory Conditions. *Corros. Sci.* **2024**, *240*, 112451. [CrossRef]
22. Bici, M.; Brischetto, S.; Campana, F.; Ferro, C.G.; Seclì, C.; Varetti, S.; Maggiore, P.; Mazza, A. Development of a Multifunctional Panel for Aerospace Use Through SLM Additive Manufacturing. *Procedia CIRP* **2018**, *67*, 215–220. [CrossRef]
23. Ferro, C.G.; Varetti, S.; Maggiore, P.; Lombardi, M.; Biamino, S.; Manfredi, D.; Calignano, F. Design and Characterization of Trabecular Structures for an Anti-Icing Sandwich Panel Produced by Additive Manufacturing. *J. Sandw. Struct. Mater.* **2020**, *22*, 1111–1131. [CrossRef]
24. Guo, H.; Wang, H.; Li, X.; Dong, Z.; Zhang, L.; Li, W. Investigation of Mechanical Properties of Laser Powder Bed Fused AlSi10Mg Lattice Structures Using GTN Damage Model. *J. Mater. Res. Technol.* **2024**, *29*, 1937–1948. [CrossRef]
25. Mines, R.A.W.; Tsopanos, S.; Shen, Y.; Hasan, R.; McKown, S.T. Drop Weight Impact Behaviour of Sandwich Panels with Metallic Micro Lattice Cores. *Int. J. Impact Eng.* **2013**, *60*, 120–132. [CrossRef]
26. Hou, S.; Li, T.; Jia, Z.; Wang, L. Mechanical Properties of Sandwich Composites with 3d-Printed Auxetic and Non-Auxetic Lattice Cores Under Low Velocity Impact. *Mater. Des.* **2018**, *160*, 1305–1321. [CrossRef]
27. Acanfora, V.; Zarrelli, M.; Riccio, A. Experimental and Numerical Assessment of the Impact Behaviour of a Composite Sandwich Panel with a Polymeric Honeycomb Core. *Int. J. Impact Eng.* **2023**, *171*, 104392. [CrossRef]
28. Wu, Q.; Gao, Y.; Wei, X.; Mousanezhad, D.; Ma, L.; Vaziri, A.; Xiong, J. Mechanical Properties and Failure Mechanisms of Sandwich Panels with Ultra-Lightweight Three-Dimensional Hierarchical Lattice Cores. *Int. J. Solids Struct.* **2018**, *132–133*, 171–187. [CrossRef]
29. Arputharaj, J.D.; Nafisi, S.; Ghomashchi, R. Compression Behaviour of L-PBF-Manufactured Ti6Al4V BCC Lattices. *Metals* **2025**, *15*, 220. [CrossRef]
30. Güden, M.; Alpkaya, A.T.; Hamat, B.A.; Hızlı, B.; Taşdemirci, A.; Tanrıkulu, A.A.; Yavaş, H. The Quasi-Static Crush Response of Electron-Beam-Melt Ti6Al4V Body-Centred-Cubic Lattices: The Effect of the Number of Cells, Strut Diameter and Face Sheet. *Strain* **2022**, *58*, e12411. [CrossRef]
31. Mazur, M.; Leary, M.; Sun, S.; Vcelka, M.; Shidid, D.; Brandt, M. Deformation and Failure Behaviour of Ti-6Al-4V Lattice Structures Manufactured by Selective Laser Melting (SLM). *Int. J. Adv. Manuf. Technol.* **2015**, *84*, 1391–1411. [CrossRef]
32. Buffa, G.; Costa, A.; Palmeri, D.; Pollara, G.; Fratini, L. Defining a New Process Window for LPBF of Ti-6Al-4V Based on Micro-Warping Phenomena. *CIRP J. Manuf. Sci. Technol.* **2024**, *52*, 1–11. [CrossRef]
33. Palmeri, D.; Pollara, G.; Licari, R.; Micari, F. Finite Element Method in L-PBF of Ti-6Al-4V: Influence of Laser Power and Scan Speed on Residual Stress and Part Distortion. *Metals* **2023**, *13*, 1907. [CrossRef]
34. Peter, N.; Pitts, Z.; Thompson, S.; Saharan, A. Benchmarking Build Simulation Software for Laser Powder Bed Fusion of Metals. *Addit. Manuf.* **2020**, *36*, 101531. [CrossRef]
35. Gouge, M.; Michaleris, P.; Denlinger, E.; Irwin, J. The Finite Element Method for the Thermo-Mechanical Modeling of Additive Manufacturing Processes. In *Thermo-Mechanical Modeling of Additive Manufacturing*; Elsevier: Amsterdam, The Netherlands, 2017; pp. 19–38. ISBN 9780128118207.
36. Sih, S.S.; Barlow, J.W. The Prediction of the Emissivity and Thermal Conductivity of Powder Beds. *Part. Sci. Technol.* **2004**, *22*, 427–440. [CrossRef]
37. Li, C.; Gouge, M.F.; Denlinger, E.R.; Irwin, J.E.; Michaleris, P. Estimation of Part-to-Powder Heat Losses as Surface Convection in Laser Powder Bed Fusion. *Addit. Manuf.* **2019**, *26*, 258–269. [CrossRef]
38. Gouge, M.; Denlinger, E.; Irwin, J.; Li, C.; Michaleris, P. Experimental Validation of Thermo-Mechanical Part-Scale Modeling for Laser Powder Bed Fusion Processes. *Addit. Manuf.* **2019**, *29*, 100771. [CrossRef]
39. Liu, X.; Wada, T.; Suzuki, A.; Takata, N.; Kobashi, M.; Kato, M. Understanding and Suppressing Shear Band Formation in Strut-Based Lattice Structures Manufactured by Laser Powder Bed Fusion. *Mater. Des.* **2021**, *199*, 109416. [CrossRef]
40. Pattillo, P.D. Column Stability. In *Elements of Oil and Gas Well Tubular Design*; Elsevier: Amsterdam, The Netherlands, 2018; pp. 273–313.

41. Kelly, C.N.; Kahra, C.; Maier, H.J.; Gall, K. Processing, Structure, and Properties of Additively Manufactured Titanium Scaffolds with Gyroid-Sheet Architecture. *Addit. Manuf.* **2021**, *41*, 101916. [CrossRef]
42. Leuders, S.; Thöne, M.; Riemer, A.; Niendorf, T.; Tröster, T.; Richard, H.A.; Maier, H.J. On the Mechanical Behaviour of Titanium Alloy TiAl6V4 Manufactured by Selective Laser Melting: Fatigue Resistance and Crack Growth Performance. *Int. J. Fatigue* **2013**, *48*, 300–307. [CrossRef]